Ambient seismic noise image of the structurally-controlled heat and fluid feeder pathway at Campi Flegrei caldera

L. De Siena,[1]

C. Sammarco,[1]

D. G. Cornwell,[1]

M. La Rocca,[2]

F. Bianco,[3]

L. Zaccarelli,[4]

H. Nakahara[5]

L. De Siena, Department of Geology and Petroleum Geology, School of Geosciences, University of Aberdeen, Meston Building, King's College, Aberdeen AB24 3UE Scotland, UK (lucadesiena@abdn.ac.uk)

C. Sammarco, Department of Geology and Petroleum Geology, School of Geosciences, University of Aberdeen, Meston Building, King's College, Aberdeen AB24 3UE Scotland, UK

D. G. Cornwell, Department of Geology and Petroleum Geology, School of Geosciences, University of Aberdeen, Meston Building, King's College, Aberdeen AB24 3UE Scotland, UK

M. La Rocca, Dipartimento di Biologia, Ecologia e Scienze della Terra, Università della Calabria, Italy

F. Bianco, Istituto Nazionale di Geofisica e Vulcanologia, Sezione di Napoli-Osservatorio Vesuviano, Via Diocleziano 328, 80124 Napoli, Italy

L. Zaccarelli, Istituto Nazionale di Geofisica e Vulcanologia, Sezione di Bologna, Bologna, Italy

H. Nakahara, Department of Geophysics, Graduate School of Science, Tohoku University, 6-3, Aramaki-Aza-Aoba, Aoba-ku, Sendai 980-8578, Japan

[1]Department of Geology and Petroleum

Geology, School of Geosciences, University of Aberdeen, Meston Building, King's College, Aberdeen AB24 3UE Scotland, UK

[2]Dipartimento di Biologia, Ecologia e Scienze della Terra, Università della Calabria, Italy

[3]Istituto Nazionale di Geofisica e Vulcanologia, Sezione di Napoli-Osservatorio Vesuviano, Via Diocleziano 328, 80124 Napoli, Italy

[4]Istituto Nazionale di Geofisica e Vulcanologia, Sezione di Bologna, Bologna, Italy

[5]Department of Geophysics, Graduate School of Science, Tohoku University, 6-3, Aramaki-Aza-Aoba, Aoba-ku, Sendai 980-8578, Japan

Key Points.

- Rayleigh-wave tomography of Campi Flegrei caldera using three years of continuous ambient seismic noise data;
- Low velocities map an aseismic reservoir feeding heat and fluids to the shallow hydrothermal during the 2011-2013 deformation unrest;
- High-velocity intra-crater domes and structural faults control reservoir extension and fluid migrations.

Earthquakes at Campi Flegrei have been low-magnitude and sparse for more than thirty years, denying onshore monitoring observations of their usual source for structural constraint: seismic tomography. Here, we used ambient seismic noise recorded between 2011 and 2013 to reconstruct period-dependent Rayleigh-wave velocity maps of caldera-wide structures and volcanic reservoirs. The lowest velocities have been aseismic since 1985 and correspond to a fluid-storage zone that was fractured during the 1983-1984 volcanic unrest. Earthquake locations show that fluids migrate from the reservoir towards the Solfatara and Pisciarelli

fumaroles along shallower low-velocity fractures. The Neapolitan Yellow Tuff rim faults bound high-velocity intra-crater domes, a product of historical eruptions, which act as a barrier for deep fluid migrations. The structurally-controlled reservoir is likely the shallowest product of a deep-seated offshore source SE of it, causing bradyseism and heating the caldera. The spatial correlations with regional ongoing dynamics and observations from historical unrests mark the reservoir as the most likely feeder pathway for fluid and magmatic inputs from this source.

1. Introduction

Thousands of microearthquakes associated with strong deformation [eg *Bellucci et al.*, 2006] and variations in geochemical gas composition [*Chiodini et al.*, 2015] spread across Campi Flegrei caldera in 1983-1984. The seismic unrest stopped at the end of 1984 due to the opening of a ∼2.5 km deep low-velocity and high-attenuation fluid reservoir [*Vanorio et al.*, 2005; *De Siena et al.*, 2017]. This reservoir intersected the structurally-defined area of cumulative pre-eruptive uplift between 1251 and 1536 AD [*Bellucci et al.*, 2006; *Di Vito et al.*, 2016] and was affected by day-long seismic injections from depth throughout the unrest [*De Siena et al.*, 2017]. Since the end of the unrest, seismicity remains low-magnitude and sparse in the caldera [eg *Di Luccio et al.*, 2015], while deformation and gas indicators have shown signals of magmatic unrests [*Amoruso et al.*, 2014b; *Trasatti et al.*, 2015; *Chiodini et al.*, 2015]. As these indicators also suggest an approach to eruption conditions [*Chiodini et al.*, 2016; *Kilburn et al.*, 2017], it is central to understand and model both seismic structures and patterns.

The scarce post-1984 seismicity may be a manifestation of changes in the caldera rheological characteristics [*Di Luccio et al.*, 2015]; scientists are already developing alternative earthquake-related strategies, more suitable to monitor such media and assess regional hazard [*Chiodini et al.*, 2017]. An alternative to earthquake monitoring is to model noise-dependent velocity variations, which are connected with volcanic unrest and eruptions [*Brenguier et al.*, 2008]. Seismic noise recorded contemporaneously at two seismic stations for a sufficient amount of time can be inverted for fundamental-mode Rayleigh wave velocity along the two station paths [*Curtis et al.*, 2006]. The Osservatorio Vesuviano has

thus acquired and stored ambient seismic noise at its temporary stations (Fig. 1a, grey triangles) since 2007 to monitor the caldera elastic properties using noise-derived velocity variations [*Zaccarelli and Bianco*, 2017]. The results of this analysis are compatible with the occurrence of a magmatic intrusion on September 7, 2012 [*D'Auria et al.*, 2015], producing a deep, intense seismic swarm. After 2011, velocity variations are also correlated with geochemical [*Chiodini et al.*, 2015, 2016] and deformation [*Amoruso et al.*, 2014b; *Trasatti et al.*, 2015] models, showing a gradual heating of the hydrothermal systems, induced by a magmatic source deeper than 2 km.

Seismic imaging was crucial to understand if such sources exist, where they could be located, and how their dynamics may develop during the 1983-84 unrest [*Aster and Meyer*, 1988; *Vanorio et al.*, 2005; *Tramelli et al.*, 2006; *De Siena et al.*, 2017]; the derived models led to an intense debate about the nature of the unrest source (fluid or magmatic) [*Amoruso et al.*, 2014a; *Vanorio and Kanitpanyacharoen*, 2015]. Active data recorded by the SERAPIS experiment (2001) have updated the structural models of the caldera after 1984 only offshore Pozzuoli (Fig. 1a, **P**) [*Battaglia et al.*, 2008; *Zollo et al.*, 2008; *Serlenga et al.*, 2016]. The lack of a widely distributed post-1984 seismicity precludes imaging of the onshore caldera structures, a better understanding of the post-1984 unrest dynamics, and a full assessment of the related hazards. The same noise dataset can be used to track the fundamental Rayleigh mode in the caldera and perform surface-wave tomography [*Brenguier et al.*, 2007; *Jaxybulatov et al.*, 2014]. An application of this technique to the region using three months of noise-data recorded in 2010 shows positive correlations

of velocity anomalies with pre-existing travel-time tomography and stratigraphy models [*Costanzo et al.*, 2017].

Here, the seismic noise dataset recorded between January 2011 and December 2013 is used to provide the first high-resolution seismic velocity image of Campi Flegrei during a full post-1984 deformation unrest [*Amoruso et al.*, 2014b]. By mapping seismic group velocities in the shallow caldera crust we can infer structural and unrest characteristics, as variations in velocity anomalies are typically related to geological boundaries and fluid and magma contents [*Brenguier et al.*, 2007; *Jaxybulatov et al.*, 2014; *Sammarco et al.*, 2017]. Seismic noise processing uses linear and phase-weighted stacking [*Schimmel and Gallart*, 2007] and takes into consideration both the anisotropic behaviour of noise sources and seismic scattering [*Tramelli et al.*, 2006; *De Siena et al.*, 2013; *De Lauro et al.*, 2013]. An advanced framework for surface wave tomography imaging [*Dziewonski et al.*, 1969; *Herrmann*, 2013; *Rawlinson and Kennett*, 2008; *Sammarco et al.*, 2017] provides group velocity maps between periods of 0.9 s and 2 s. The comparison with the best-localised microearthquakes nucleated in 1983-1984 and 2005-2016 [*Lomax et al.*, 2001], recent and historical spatial deformation measurements [*Bellucci et al.*, 2006; *Woo and Kilburn*, 2010; *Di Vito et al.*, 2016] and tectonic boundaries and geomorphology [*Vilardo et al.*, 2013; *Vitale and Isaia*, 2014] unveils the shallowest manifestations of the Campi Flegrei heat and fluid feeder pathways.

2. Data and methods

2.1. Anisotropic seismic noise data and cross-correlations

The input data for ambient noise tomography is a seismic noise dataset recorded at the temporary network of the Osservatorio Vesuviano (Fig. 1a) between 2011 and 2013 [*La Rocca and Galluzzo*, 2015]. To assess the quality of the dataset and the frequency band to analyse we plotted (Fig. S1): noise-data availability; the cumulative number of stations per month; a comparison of the power spectral densities calculated at each station over one month of data with the low and high models defined by *Peterson* [1993]. We only selected the 12 stations recording at least one year of seismic noise, as shorter periods would deteriorate cross-correlation stability [*Curtis et al.*, 2006; *Bensen et al.*, 2007]. The frequency band where we expect to retrieve good cross correlations is between 0.1 Hz and 1.5 Hz (Fig. S1, lowest panel). Between 0.2 Hz and 1 Hz, an additional stationary semi-circularly-polarised source located at Solfatara (Fig. 1a, **S**) [*De Lauro et al.*, 2013] may affect our measurements; however, the sea and (to a much lesser extent) the weather, likely produce background noise at these frequencies [*La Rocca and Galluzzo*, 2015].

Empirical Green's functions (EGF) are obtained by cross-correlating ambient seismic noise recorded at station pairs with the data processing described by *Bensen et al.* [2007]. After the removal of instrument response, mean and trend, we down-sampled noise data at each station to ten samples per seconds hour-long time series of the vertical component of ground motion. High-pass filtering at 0.1 Hz, temporal normalisation and spectral whitening lower the effect of earthquake signals and spikes. We cross-correlate all simultaneously-recording station pairs and produce daily and full-recording period stacks using both linear (Fig. 1b) and phase-weighted stacks [*Schimmel and Gallart*, 2007] of

order two (PWS - Fig. 1c). Station pairs separated by less than one wavelength (∼1 km) [*Luo et al.*, 2015] or showing no EGFs were discarded. Because of the constraints on station distances and the quality of noise recordings the only frequency band suitable for our analysis is 0.4-1.3 Hz.

The primary sources of noise at Campi Flegrei in this frequency band are located at the seashore; this is evident once we compare linear EGFs at pairs with different geometries but similar inter-station distances (∼2 km - Fig. S2). The CELG-GAE2 and CELG-ASB2 EGFs (Fig. S2, red) show a much stronger causal component due to their proximity to the southern shore. West-east pairs (Fig. S2, OMN2-CELG and CELG-PESG, blue) are highly symmetric as seismic noise sources contribute equally to noise from the east and the west of the array. While EGFs retrieved at ∼0.7 Hz (0.4-1 Hz) are visible with a linear stack, at ∼1 Hz (0.7-1.3 Hz) PWS is necessary to see the signal (compare Fig. 1b,c). These changes in scattering properties at different inter-station distances and frequencies, and, especially, noise source anisotropy reduce symmetry in the cross-correlations, increasing either the causal or the acausal components. By assuming symmetry of the causal and acausal EGFs [*Bensen et al.*, 2007], the noise source anisotropy would limit the efficient reconstruction of the velocity anomalies, increasing biases in group-dispersion pickings. We thus selected the PWS EGFs stacking either the symmetric (average), causal, or acausal component, depending on the pair geometry, quality of the final EGF and dispersion behaviour (Fig. S3). The final version of phase-weighted stacked EGFs with respect to distance is shown in Figure 1d. We mark the fundamental mode of the Rayleigh wave travelling across the array with velocities of 0.3-2.5 km/s (red lines). An additional mode

propagates with similar velocities after 7 km inter-station distance, likely due to lateral high-impedance contrasts related to the rim [*Tramelli et al.*, 2006].

2.2. Group velocity dispersions and maps

Part of the Computer Programs for Seismology (CFS) package [*Herrmann*, 2013] was used to compute dispersion curves and automatically pick peak amplitudes (red dots with corresponding full uncertainty) necessary to perform Rayleigh-wave tomography; when possible, picks were benchmarked using FTAN [*Dziewonski et al.*, 1969]. We show four sample cross-correlations and corresponding group velocity dispersions analyses with qualities spanning from A (CFS picks agree with FTAN) to D (CFS velocity picks undetected or too low to be a surface wave) in Fig. S3. Between 0.4 and 1.3 Hz, we keep station pairs of quality A and B (clear fundamental mode recognised by CFS). The C-group velocities typically show two different velocity trends in the target frequency band (Fig. S3); in the final selection (ABCv2), we re-picked the C-curves manually and discarded pairs of quality D.

The above-mentioned processing is necessary to obtain reliable group velocity maps (Fig. 2a) at periods 0.9 s, 1.2 s, 1.5 s, and 2.0 s; these are extracted with the iterative nonlinear tomography scheme devised by *Rawlinson and Kennett* [2008]. The scheme solves the forward problem of travel-time prediction using the Fast Marching Method and a subspace inversion technique to adjust model parameters to satisfy data observations. It assumes that the geometric spreading of surface waves as a function of phase is equivalent to that of the group at a given period. The code produces models using smoothly varying cubic B-spline functions in the velocity continuum, controlled by a regular grid of 50 m-spaced

nodes in X and Y directions. Recovery and model resolution were investigated using a checkerboard test, with an input model comprising alternating 2-km-spaced velocity anomalies of 0.5 km/s and 2 km/s. Figs. S4-S9 (plotted with GMT) show how the three different data selections (AB, ABC, and ABCv2) affected checkerboard testing (Fig. S4), inverted patterns with different parametrisations (Figs. S5-S7, also showing ray paths used to reconstruct the anomalies and the relative location of seismic stations) and residual reduction (Fig. S8). The final ABCv2 velocity maps were imported into the *Voxler*© environment and overlain with available tectonic and seismicity information [*Isaia et al.*, 2009; *Vilardo et al.*, 2013; *Vitale and Isaia*, 2014; *De Siena et al.*, 2017]. We only interpret anomalies that are consistent between the ABC and ABCv2 datasets, generally reproduced onshore, inside and on the Neapolitan Yellow Tuff rim (Fig. 2 and 3a-d- bright colours).

2.3. Microearthquake localisations

Seismic locations provide both an insight into fluid and magma migration and volcano dynamics and an improved characterisation of the velocity anomalies. We use the NonLinLoc software [*Lomax et al.*, 2001] with the Oct-Tree algorithm to obtain microearthquake locations for the period 2005-2016. The inputs are the 3-D P- and S-wave velocity models of *Battaglia et al.* [2008] and routine manual picks performed by the Osservatorio Vesuviano at its permanent and mobile seismic stations (see *Chiodini et al.* [2017], Fig. 1, for a map of the array). We have obtained $\sim$ 400 maximum likelihood localisations (Fig. 3b,c,e,f) having a minimum of eight picks, an average root mean square travel-time residual of 0.05 s, maximum gap of 85 degrees, and a single spatial maximum in the mapped full probability density distributions (red dots, Fig. S5), respectively.

3. Results

In the 2-s panel of Fig. 2 we highlight the spatial correlation of the velocity anomalies with local and regional tectonic structures. At all periods, an aseismic low-velocity structure related to infills in the eastern part of the caldera (Fig. 2a-d) is dampened at 2 s, and connected at 0.9 s to the central low-velocity zone. The lowest velocities are always located between Monte Nuovo (**M**), Monte Gauro, and Solfatara (Fig. 3a-d) and intersect the crossing of La Starza marine terrace with two significant SN and SSW-NNE directed faults. Considering the 1D S-wave velocity model used by *Battaglia et al.* [2008], group velocities at 2 s are theoretically sensitive to structures as deep as 2.5 km. At these depths, high-velocity areas contour the 2-s low-velocity anomaly to the west, north and east. These high-velocity zones shrink at lower periods, progressively opening low-velocity pathways towards Monte Nuovo, Solfatara, and east of Monte Gauro (Fig. 2, 0.9-1.5 s).

Fig. 3a-h zooms on the resolved 2 s (left) and 0.9 s (right) group velocity maps; different geophysical and tectonic information overlay each panel for interpretation. The area delineated by the broken line (Fig. 3a,b) accounts for 95% of the seismicity induced by day-long injections throughout the 1983-84 unrest [*De Siena et al.*, 2017]: these injections and the low-velocity anomaly are located NW of the centre of the main deformation anomaly modelled between 2011 and 2013 (**x**, [*Amoruso et al.*, 2014b]). The 2005-2016 hypocentres (Fig. 3c,d) spread between depths of 0 and 2 km and contour the eastern side of the 2-s anomaly, clustering east of the Solfatara crater. The deepest and highest-magnitude swarm in this period (depths of about 2.5 km, nucleated on September 7, 2012) crosses the northwestern border of the anomaly, at the opposite side of the reservoir

with respect to the deformation source (Fig. 3c). The lowest velocity anomaly at 2 s is clearly bounded by: (1) faults, manifestations of regional tectonic stress [*Woo and Kilburn*, 2010] (Fig. 3e); and (2) smaller scale pre-existing fractures to the east, associated to background seismicity [*Chiodini et al.*, 2017] (Fig. 3b). These fractures become consistently low-velocity at shallower depths (Fig. 3f). Fig. 3e,f shows from a 3D SW view how the velocity maps spatially relate to: (1) the geomorphological map of the caldera; (2) the microseismicity recorded between 2005 and 2016; and (3) the locations of two archeological markers of bradyseism: the Macellum (Temple of Serapis, purple square, a partially submerged edifice) and Portus Iulius (a submerged roman port abandoned in the IV century).

3.1. Discussion

The fluid storage and production zone feeding shallow hydrothermals at Campi Flegrei [*Vanorio et al.*, 2005; *De Siena et al.*, 2017] is still the most distinct seismic velocity feature in 2011-2013 (Fig. 3, left). Day-long NW-directed seismic swarms throughout 1983 and until April 1, 1984 (Fig. 3a) were manifestations of either a dyke intrusion or repeated fluid injections from a SE high attenuation and deformation source [*Woo and Kilburn*, 2010; *Amoruso et al.*, 2014b; *De Siena et al.*, 2017]. The only relevant seismic swarm detected between 2011 and 2013 nucleated on September 7, 2012 (Fig. 3c,e). It is deeper (e.g. Fig. 3e) and higher magnitude with respect to the background seismicity, and on the opposite side of the reservoir with respect to the point of maximum deformation (**x**, Fig. 3a,c): we thus infer that the dynamics affecting the reservoir are still SE-to-NW-directed and structurally controlled by regional stress, as in 1983-84 [*Woo and Kilburn*, 2010]. As

heat is increasing in upper hydrothermal [*Chiodini et al.*, 2016], the reservoir is its most likely feeder pathway of both fluids and heat.

The spatial location of the 2-s low-velocity anomaly with respect to seismicity confirms that this structure is still feeding the shallower hydrothermal; but why did the reservoir become aseismic between 2005 and 2016 (Fig. 3b) and before, since 1985 [*Di Luccio et al.*, 2015]? The cause can be traced in the April 1, 1984 injection from depth. It marked a drastic permeability change in the reservoir, making it subject to aseismic slip for almost two months [*De Siena et al.*, 2017]. Hundreds of micro-earthquakes spread from the reservoir from this date, crossing structural faults in the western caldera and, for the first time during the unrest, the region of the 1538 AD Monte Nuovo eruption. The dynamics of the 1984 seismic unrest in the reservoir support the view of a change in the rheological characteristics of the caldera [*Di Luccio et al.*, 2015]. The reservoir is the area most affected by this change; while deformation observations can be explained by decarbonation reaction at its base [*Vanorio and Kanitpanyacharoen*, 2015], a likely source in 2011-2013 is a degassing magmatic source located SE and below the mapped anomaly [*Amoruso et al.*, 2014b; *Chiodini et al.*, 2016]. The drastic changes affecting the reservoir, its geometry with respect to historical magmatic sources of deformation, tectonic structures, and archaeological building marked by past bradyseisms (Fig. 3e,f) thus strongly hint at a central role of the reservoir area as point of release of continuous regionally-driven [*Woo and Kilburn*, 2010] SE-to-NW-directed magmatic dynamics [eg *Di Vito et al.*, 2016].

These historical and pre-historical dynamics have shaped the caldera structure and produce clear high-velocity anomalies, which constrain the deep reservoir and hazardous fluid migrations (Fig. 3b,c). Three separated deep high-velocity structures (Fig. 3c) are contoured by the faults bordering the Neapolitan Yellow Tuff rim, recognised as the main high-velocity, low-attenuation, and high-scattering structure by previous studies [*Vanorio et al.*, 2005; *Tramelli et al.*, 2006; *Battaglia et al.*, 2008; *De Siena et al.*, 2011; *Serlenga et al.*, 2016; *Costanzo and Nunziata*, 2017]. The PWS EGFs at $\sim$1 Hz show similar causal and acausal components for inter-station distances up to 7 km (Fig. 1c), which is the approximate diameter of the Neapolitan Yellow Tuff rim. The high lateral impedance contrast and diffusive characteristics of this scattering anomaly in the caldera [*Tramelli et al.*, 2006; *De Siena et al.*, 2013] are the most likely source of the second mode, which propagates with a velocity similar to that of the original source. However, the comparison with the Campi Flegrei stratigraphy [*Isaia et al.*, 2009] and morphometry [*Vilardo et al.*, 2013] highlights that the separated high-velocity structures are most likely manifestations of intra-crater residual of plumbing systems, older than 8.2 ka. These plumbing systems and the associated caldera-bounding faults have played, and still play, a central role in driving magmatism and fluid circulation in the shallow caldera.

The understanding of the hazard posed by the feeder pathway must take into account these velocity constraints to fluid migration, the presence of an extended highly-deforming caprock [*Vanorio and Kanitpanyacharoen*, 2015] and, especially, the background shallow seismicity to the east of the reservoir (Fig. 3b,f). Here, seismic low velocities that connect the reservoir to the eastern low-velocity caldera infills are in fact compatible with the

reactivation of the preexisting fractures, resulting from an increase in injection-induced pore pressure and heat [*Chiodini et al.*, 2017; *Kilburn et al.*, 2017]. Fluids produced by the hydrothermal feeder are thus bound to travel towards Pisciarelli, where new geyser-like vents started opening in 2013 [*Chiodini et al.*, 2015], following pathways parallel to the one connecting the two main sources of deformation [*Amoruso et al.*, 2014a]. The results thus support the assessment of the eastern caldera as the zone of highest probability of vent opening [*Bevilacqua et al.*, 2015], fed through the deeper low-velocity reservoir.

The nature of the reservoir cannot be discriminated just by its low-velocity characteristics. The reservoir could either be filled by lime-rich fluids derived from hydrothermal decarbonation reactions of the basement [eg *Vanorio and Kanitpanyacharoen*, 2015] or by magmatic fluids whose source is located SE of the reservoir [eg *Amoruso et al.*, 2014b]. Given the uncertainty associated to the depth of the 2-s velocity map, it could even be the top of the magmatic injection modelled under the urban area of Naples *D'Auria et al.* [2015]. The limitations of our technique do not allow to completely remove biases produced by noise sources (Fig. S2) and more advanced techniques like multi-dimensional deconvolution [*Wapenaar et al.*, 2011] may better model absolute velocity values, thus improving characterisation of the reservoir. We infer the presence of magmatic fluids in the reservoir due to the aseismicity of the reservoir and the earthquake geometry around it. Driven by ongoing tectonics [*Woo and Kilburn*, 2010], the stable magmatic deformation source SE of the reservoir is still the deepest trigger of the unrest, and likely produces the September 7, 2012 swarm located just opposite to the source. Fluid injections from this source may induce thermal processes and aseismic plastic shear strain in the colder

hydrothermal reservoir, as observed during stimulation at The Geyser Geothermal field (US - [*Jeanne et al.*, 2015]): the seismicity east of the reservoir would be a consequence of the reactivation of the pre-existent fractures, due to an increase in injection-induced pore pressure.

4. Conclusions

Ambient seismic noise imaging is the primary available seismic imaging method at Campi Flegrei due to the absence of consistent well-spread seismicity since December 1984. The results of its application to three years of seismic noise data recorded during unrest (2011-2013) show that the lowest velocities are between Monte Gauro, Pozzuoli and Monte Nuovo, and cross La Starza marine terrace. The deepest low-velocity anomaly corresponds to the seismically-active reservoir that was fractured during the 1983-84 unrest; the same area is aseismic since at least 2005. Both ancient plumbing systems inside the Neapolitan Yellow Tuff rim and SE-to-NW-directed tectonic structures in the caldera centre constrain this heat and hydrothermal feeder pathway. The high-velocity structures act as a barrier for deep northward and westward fluid migrations. The shallow low-velocity anomalies in the eastern caldera are seismically active; this is a signature of heated hazard-prone hydrothermal systems, fed by the deeper reservoir, and bound to propagate towards the Pisciarelli fumarole fields via pre-existent fractures and faults.

The structurally-controlled reservoir is in spatial relation with historical pre-eruptive deformation and archaeological records of bradyseism. Its location with respect to deformation anomalies, seismicity, and observations of historical unrests supports the existence of an ongoing NW-directed feeding dynamic controlled by regional tectonics. The reser-

voir is still low velocity as in 1983-84 but the absence of internal seismicity, increase in caldera temperature, and distribution of earthquakes around it are evidence of a change in the caldera's post-1984 characteristics. We infer that fluid and magmatic inputs from the deeper magmatic source are still likely to enter the shallower crust from this feeder pathway.

Acknowledgments. The Japan Society for the Promotion of Science - Short-Term Fellowship (JSPS/OF215/022) financed this work. We thank Giuseppe Vilardo and Eliana Bellucci Sessa for providing the geomorphological maps, and Simona Petrosino and Paola Cusano for the P- and S-wave pickings used to localise the seismicity. Informal revisions from Guido Ventura, Nick Rawlinson and Chris Kilburn helped us improving the analyses and interpretation, respectively. We acknowledge the help of Naveed Khan in parallelising the codes. Velocity maps and seismic locations are stored in the World Data Center PANGAEA. Correspondence and requests for materials should be addressed to Luca De Siena.

References

Amoruso, A., L. Crescentini, and I. Sabbetta, Paired deformation sources of the campi flegrei caldera (italy) required by recent (1980–2010) deformation history, *Journal of Geophysical Research: Solid Earth*, *119*(2), 858–879, 2014a.

Amoruso, A., L. Crescentini, I. Sabbetta, P. De Martino, F. Obrizzo, and U. Tammaro, Clues to the cause of the 2011–2013 Campi Flegrei caldera unrest, Italy, from continuous GPS data, *Geophysical Research Letters*, *41*(9), 3081–3088, 2014b.

Aster, R., and R. Meyer, Three dimensional velocity structure and hypocenter distribution in the campi flegrei caldera, italy, *Tectonophysics*, *149*, 195–218, 1988.

Battaglia, J., A. Zollo, J. Virieux, and D. Dello Iacono, Merging active and passive data sets in traveltime tomography: the case study of Campi Flegrei caldera (Southern Italy), *Geophysical Prospecting*, *56*, 555–573, 2008.

Bellucci, F., J. Woo, C. R. Kilburn, and G. Rolandi, Ground deformation at Campi Flegrei, Italy: implications for hazard assessment, *Geological Society, London, Special Publications*, *269*(1), 141–157, 2006.

Bensen, G. D., M. H. Ritzwoller, M. P. Barmin, A. L. Levshin, F. Lin, M. P. Moschetti, N. M. Shapiro, and Y. Yang, Processing seismic ambient noise data to obtain reliable broad-band surface wave dispersion measurements, *Geophysical Journal International*, *169*, 1239–1260, 2007.

Bevilacqua, A., et al., Quantifying volcanic hazard at Campi Flegrei caldera (Italy) with uncertainty assessment: 1. Vent opening maps, *Journal of Geophysical Research: Solid Earth*, *120*(4), 2309–2329, 2015.

Brenguier, F., N. M. Shapiro, M. Campillo, A. Nercessian, and V. Ferrazzini, 3-D surface wave tomography of the Piton de la Fournaise volcano using seismic noise correlations, *Geophysical Research Letters.*, *34*(L02305), doi:10.1029/2006GL028,586, 2007.

Brenguier, F., N. M. Shapiro, M. Campillo, V. Ferrazzini, Z. Duputel, O. Coutant, and A. Nercessian, Towards forecasting volcanic eruptions using seismic noise, *Nature Geoscience*, *January*, doi :10.1038/ngeo104, 2008.

Chiodini, G., J. Vandemeulebrouck, S. Caliro, L. D'Auria, P. De Martino, A. Mangiacapra, and Z. Petrillo, Evidence of thermal-driven processes triggering the 2005–2014 unrest at Campi Flegrei caldera, *Earth and Planetary Science Letters*, *414*, 58–67, 2015.

Chiodini, G., A. Paonita, A. Aiuppa, A. Costa, S. Caliro, P. De Martino, V. Acocella, and J. Vandemeulebrouck, Magmas near the critical degassing pressure drive volcanic unrest towards a critical state, *Nature Communications*, *7*, 13,712, 2016.

Chiodini, G., et al., Clues on the origin of post-2000 earthquakes at Campi Flegrei caldera (Italy), *Scientific reports*, *7*, 2017.

Costanzo, M., and C. Nunziata, Inferences on the lithospheric structure of Campi Flegrei District (southern Italy) from seismic noise cross-correlation, *Physics of the Earth and Planetary Interiors*, *265*, 92–105, 2017.

Costanzo, M., C. Nunziata, and R. Strollo, VS of the uppermost crust structure of the Campi Flegrei caldera (southern Italy) from ambient noise Rayleigh wave analysis, *Journal of Volcanology and Geothermal Research*, 2017.

Curtis, A., P. Gerstoft, H. Sato, R. Snieder, and K. Wapenaar, Seismic interferometry: Turning noise into signal, *The Leading Edge*, *25*(9), 1082–1092, 2006.

D'Auria, L., et al., Magma injection beneath the urban area of Naples: a new mechanism for the 2012–2013 volcanic unrest at Campi Flegrei caldera, *Scientific reports*, *5*, 2015.

De Lauro, E., S. De Martino, M. Falanga, and S. Petrosino, Synchronization between tides and sustained oscillations of the hydrothermal system of Campi Flegrei (Italy), *Geochemistry, Geophysics, Geosystems*, *14*(8), 2628–2637, 2013.

De Siena, L., E. Del Pezzo, and F. Bianco, A scattering image of Campi Flegrei from the autocorrelation functions of velocity tomograms, *Geophysical Journal International*, *184*(3), 1304–1310, 2011.

De Siena, L., E. Del Pezzo, C. Thomas, A. Curtis, and L. Margerin, Seismic energy envelopes in volcanic media: in need of boundary conditions, *Geophysical Journal International*, *192*(1), 326–345, 2013.

De Siena, L., G. Chiodini, G. Vilardo, E. Del Pezzo, M. Castellano, S. Colombelli, N. Tisato, and G. Ventura, Source and dynamics of a volcanic caldera unrest: Campi Flegrei, 1983–84, *Scientific Reports*, *7*, 2017.

Di Luccio, F., N. Pino, A. Piscini, and G. Ventura, Significance of the 1982–2014 Campi Flegrei seismicity: Preexisting structures, hydrothermal processes, and hazard assessment, *Geophysical Research Letters*, *42*(18), 7498–7506, 2015.

Di Vito, M. A., et al., Magma transfer at Campi Flegrei caldera (Italy) before the 1538 AD eruption, *Scientific Reports*, *6*, 32,245, doi:10.1038/srep32245, 2016.

Dziewonski, A., S. Bloch, and M. Landisman, A technique for the analysis of transient seismic signals, *Bulletin of the seismological Society of America*, *59*(1), 427–444, 1969.

Herrmann, R. B., Computer programs in seismology: An evolving tool for instruction and research, *Seismological Research Letters*, *84*(6), 1081–1088, 2013.

Isaia, R., P. Marianelli, and A. Sbrana, Caldera unrest prior to intense volcanism in campi flegrei (italy) at 4.0 ka bp: Implications for caldera dynamics and future eruptive scenarios, *Geophysical Research Letters*, *36*(21), 2009.

385 Jaxybulatov, K., N. Shapiro, I. Koulakov, A. Mordret, M. Landès, and C. Sens-
386 Schönfelder, A large magmatic sill complex beneath the Toba caldera, *Science*,
387 *346*(6209), 617–619, 2014.

388 Jeanne, P., J. Rutqvist, A. P. Rinaldi, P. F. Dobson, M. Walters, C. Hartline, and J. Gar-
389 cia, Seismic and aseismic deformations and impact on reservoir permeability: The case
390 of EGS stimulation at The Geysers, California, USA, *Journal of Geophysical Research:*
391 *Solid Earth*, *120*(11), 7863–7882, 2015.

392 Kilburn, C. R., G. De Natale, and S. Carlino, Progressive approach to eruption at Campi
393 Flegrei caldera in southern Italy, *Nature Communications*, *8*, 2017.

394 La Rocca, M., and D. Galluzzo, Seismic monitoring of Campi Flegrei and Vesuvius by
395 stand-alone instruments, *Annals of Geophysics*, *58*(5), S0544, 2015.

396 Lomax, A., A. Zollo, P. Capuano, and J. Virieux, Precise, absolute earthquake location
397 under somma vesuvius volcano using a new three dimensional velocity model, *Geophys-*
398 *ical Journal International*, *146*, 313–331, 2001.

399 Luo, Y., Y. Yang, Y. Xu, H. Xu, K. Zhao, and K. Wang, On the limitations of interstation
400 distances in ambient noise tomography, *Geophysical Journal International*, *201*(2), 652–
401 661, 2015.

402 Peterson, J., Observations and modeling of seismic background noise, *Tech. rep.*, US
403 Geological Survey Alburquerque, New Mexico, 1993.

404 Rawlinson, N., and B. Kennett, Teleseismic tomography of the upper mantle beneath
405 the southern Lachlan Orogen, Australia, *Physics of the Earth and Planetary Interiors*,
406 *167*(1), 84–97, 2008.

Sammarco, C., D. G. Cornwell, and N. Rawlinson, Ambient noise tomography reveals basalt and sub-basalt velocity structure beneath the Faroe Islands, North Atlantic, *Tectonophysics*, *721*, 1–11, 2017.

Schimmel, M., and J. Gallart, Frequency-dependent phase coherence for noise suppression in seismic array data, *Journal of Geophysical Research: Solid Earth*, *112*(B4), 2007.

Serlenga, V., S. Lorenzo, G. Russo, O. Amoroso, S. Garambois, J. Virieux, and A. Zollo, A three-dimensional QP imaging of the shallowest subsurface of Campi Flegrei offshore caldera, southern Italy, *Geophysical Research Letters*, *43*(21), 209–218, doi: 10.1002/2016GL071140, 2016.

Tramelli, A., E. D. Pezzo, F. Bianco, and E. Boschi, 3D scattering image of the Campi Flegrei caldera (Southern Italy). New hints on the position of the old caldera rim, *Physics of the Earth and Planetary Interiors*, *155*, 269–280, 2006.

Trasatti, E., M. Polcari, M. Bonafede, and S. Stramondo, Geodetic constraints to the source mechanism of the 2011–2013 unrest at Campi Flegrei (Italy) caldera, *Geophysical Research Letters*, *42*(10), 3847–3854, 2015.

Vanorio, T., and W. Kanitpanyacharoen, Rock physics of fibrous rocks akin to Roman concrete explains uplifts at Campi Flegrei Caldera, *Science*, *349*(6248), 617–621, 2015.

Vanorio, T., J. Virieux, P. Capuano, and G. Russo, Three-dimensional tomography from P wave and S wave microearthquake travel times and rock physics characterization of the Campi Flegrei Caldera, *Journal of Geophysical Research*, *110*, B03,201, doi: doi:10.129/2004JB003102, 2005.

Vilardo, G., G. Ventura, E. Bellucci Sessa, and C. Terranova, Morphometry of the Campi Flegrei caldera (Southern Italy), *Journal of Maps*, *9*(4), 635–640, 2013.

Vitale, S., and R. Isaia, Fractures and faults in volcanic rocks (campi flegrei, southern italy): Insight into volcano-tectonic processes, *International Journal of Earth Sciences*, *103*(3), 801–819, 2014.

Wapenaar, K., J. Van Der Neut, E. Ruigrok, D. Draganov, J. Hunziker, E. Slob, J. Thorbecke, and R. Snieder, Seismic interferometry by crosscorrelation and by multidimensional deconvolution: A systematic comparison, *Geophysical Journal International*, *185*(3), 1335–1364, 2011.

Woo, J. Y., and C. R. Kilburn, Intrusion and deformation at Campi Flegrei, southern Italy: sills, dikes, and regional extension, *Journal of Geophysical Research: Solid Earth*, *115*, B12,210, 2010.

Zaccarelli, L., and F. Bianco, Noise-based seismic monitoring of the Campi Flegrei caldera, *Geophysical Research Letters*, *44*(5), 2237–2244, doi:10.1002/2016GL072477, 2016GL072477, 2017.

Zollo, A., N. Maercklin, M. Vassallo, D. Dello Iacono, J. Virieux, and P. Gasparini, Seismic reflections reveal a massive melt layer feeding Campi Flegrei caldera, *Geophysical Research Letters*, *35*(L112306), doi:10.1029/2008GL034,242, 2008.

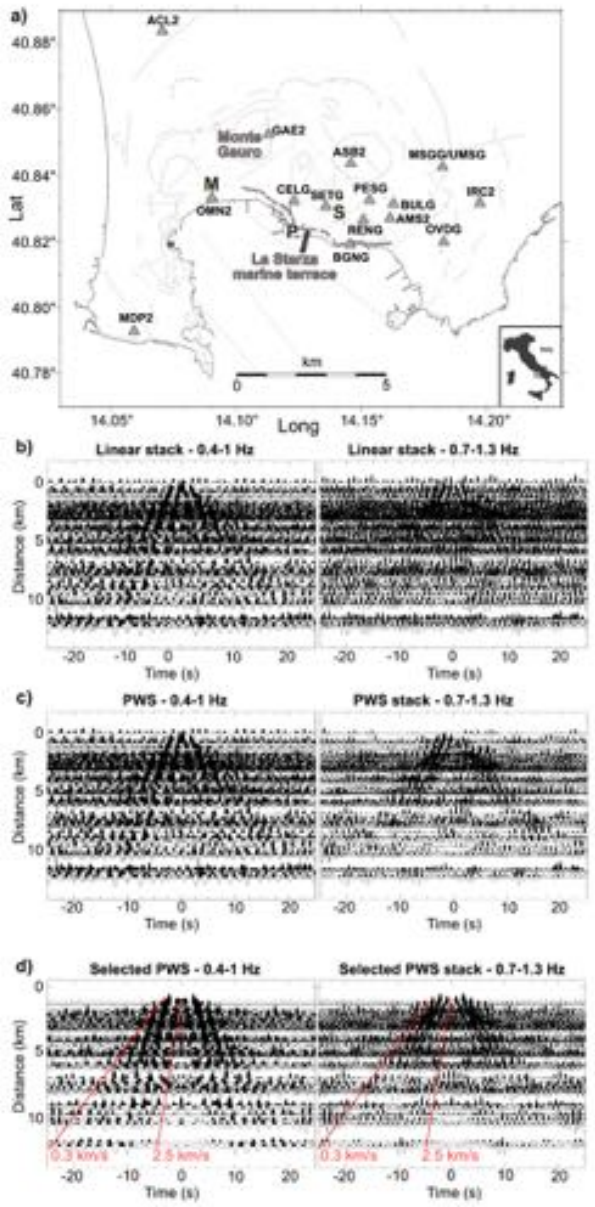

Figure 1. Seismic stations, geomorphology, and cross-correlations. (a) Seismic stations recording seismic noise during the 2011-2013 deformation unrest (grey triangles) are shown on the geomorphological map of Campi Flegrei caldera, redrawn with ArcGIS mainly from *Vilardo et al.* [2013] and *Vitale and Isaia* [2014]. (b) Cross-correlations of ambient seismic noise filtered in the two selected frequency bands using (b) linear and (c) phase-weighted stacking [*Schimmel and Gallart*, 2007]. Panel d) shows the stacked EGFs after the final selection (ABCv2). Maximum and minimum velocity are marked by dotted red lines.

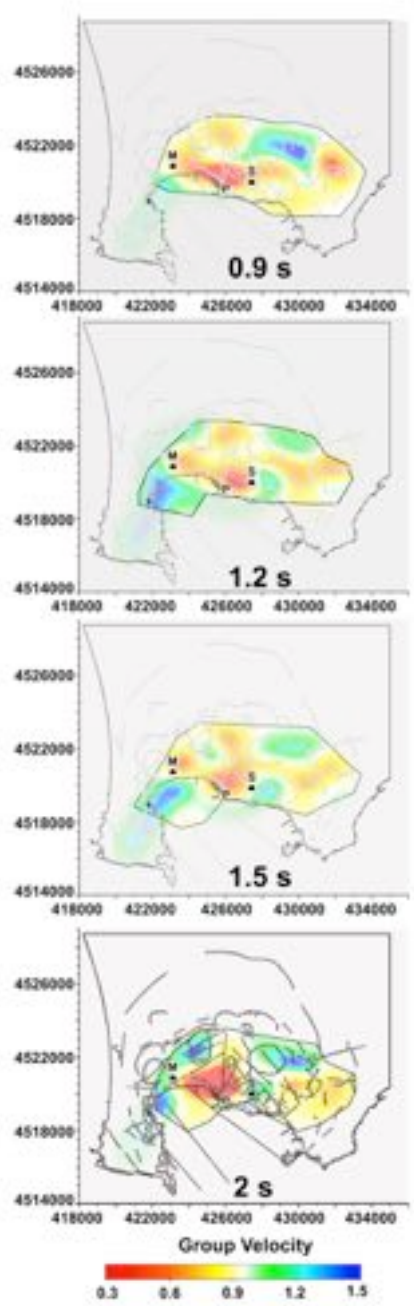

Figure 2. Ambient seismic noise-derived group velocity maps at different periods. Areas of poor or no resolution in the surface-wave velocity maps are shaded following resolution and stability tests. The pre-existing tectonic structures [*Isaia et al.*, 2009; *Vilardo et al.*, 2013; *Vitale and Isaia*, 2014] are imposed on each panel and highlighted at 2 s.

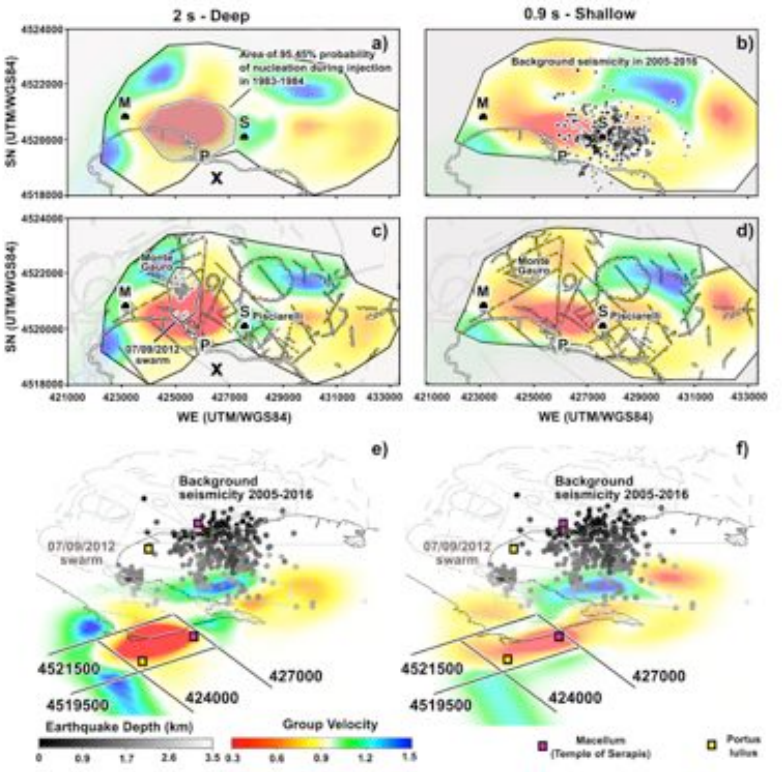

Figure 3. A comparison of the group velocity maps with seismicity and pre-existing tectonic structures. The two columns show 2-s (deep, left) and 0.9-s (shallow, right) group velocity maps. a) the shaded polyhedron and the **x** mark the area affected by the day-long 1983-84 injections [*De Siena et al.*, 2017] and the point of maximum deformation inferred by *Amoruso et al.* [2014b], respectively; b) comparison of the shallow velocity anomalies with the best-localised 2005-2016 background seismicity, coloured according to their depth; c-d) comparison of the velocity anomalies with tectonic boundaries and geomorphology. In panel c), a broken line contours the 07/09/2012 swarm. e-f) a 3D view of the tectonic boundaries and velocity anomalies from the SW at a pitch angle of 45 degrees. We include the 2005-2016 locations as well as the locations of Macellum and Portus Iulius.